Jun Liu ✉
Jiandang Xing
Xiaodong Ruan
Jian Song
Di Wu

https://doi.org/10.21278/TOF.472043022
ISSN 1333-1124
eISSN 1849-1391

ANALYSIS AND DESIGN OF THE RECONFIGURATION MOTION QUALITIES OF A DEFORMABLE ROBOT BASED ON A METAMORPHIC MECHANISM

Summary

Traditional wheel-legged ground mobile robots can only partially deform during wheel-leg switching, resulting in failure to achieve better environmental adaptability. Metamorphic mechanisms can be introduced into car structure designs. A new type of wheel-legged ground mobile robot, namely a deformable robot, is proposed in this study. Compared with traditional wheel-legged ground mobile robots, the deformable robot is capable of global reconfiguration, that is, when transitioning between the wheeled type (vehicle state) and the legged type (humanoid state), the shape, structure, degrees of freedom, and position of the centre of mass will change significantly. First, based on the characteristics of the wheel-legged compound motion, a structural model of the deformable robot was proposed and designed, and its reconfiguration motion was planned. Then, a kinematic model of the coupled reconfiguration process of the deformable robot was established. A horizontal lifting model was created to keep the front body level when lifting. The motion law of each active joint angle over time was designed based on the requirements of the reconfiguration motion smoothness. The criterion of reconfiguration stability was established and measures to improve it were proposed. Finally, based on the simulation verification of the smoothness, horizontality, and stability of the coupled reconfiguration of the system, a prototype of the deformable robot was developed, and a coupled reconfiguration experiment was conducted on an actual road surface. The experiment results show that the reconfiguration motion of the deformable robot between the vehicle state and the humanoid state had good motion qualities.

Key words: *deformable robot, kinematics analysis, reconfiguration motion, motion qualities, experimental prototype*

1. Introduction

As a type of ground mobile robot, wheel-legged robots have been widely used in military, medical, service, space exploration, and anti-riot applications [1-7]. They combine the advantages of wheeled mobile robots and legged walking robots to ensure high travel speed on a flat surface, strong terrain adaptation, and obstacle-crossing capabilities [8-13].

In terms of structural analysis, there are two types of wheel-legged robots that can achieve wheel-leg mode switching. One is to achieve wheel-leg mode switching by locking the wheels, which are installed at the end of the leg mechanism [14]. For example, Boston Dynamics developed a "Handle" robot with extreme flexibility and adaptability [15]. The robot was powered hydraulically and by a motor. Not only could it complete complex actions such as jumping, but could also drive fast in wheeled mode. The State Key Laboratory of Robotics of Harbin Institute of Technology designed a hydraulically driven biped wheel-legged WLR robot [16]. The robot could achieve complex movements such as translation and squatting. However, these two robots had a common defect: their two legs could not be separated. Therefore, they could not complete actions such as walking. Another type of robot changes the installation position of the wheels. These wheels are mounted on a fuselage or the connecting rod of the leg mechanism. Wheel-leg mode switching is performed by making the wheels touch the ground through the deformation of the mechanism. For example, the DRC-HUBO robot [17,18] was developed by the Korea Advanced Institute of Science and Technology (KAIST). Its driving wheels were added at the ankle and knee joints. The DRC-HUBO robot could not only walk with legs, but also travel with wheels in a kneeling position. However, in the case of the wheeled mode, the high position of the centre of mass made the robot unable to travel at a high speed.

The above robots were improved based on the structure of biped or multi-legged robots. However, a new type of wheel-legged ground mobile robot—the deformable robot is proposed in this paper. The wheel-legged robot introduces a metamorphic mechanism [19,20] into the vehicle design, and combines the vehicle with a biped walking robot. Compared with the traditional wheel-legged robots, the deformable robot proposed in this paper was designed based on a vehicle structure. It can not only travel in the vehicle state at a high speed on a structural road, but also stand and walk on an unstructured road when it is reconstructed into the humanoid state.

In terms of research content, traditional research on wheel-legged robots is concerned with motion analysis and control in either the wheeled or legged configurations. But little research has been done on the motion between configurations. For example, Li et al. [21] proposed a new jumping control method based on the TMS-DIP model for the stable jump of the WLR-3P robot. The method was successfully applied to the jumping process of the WLR-3P robot platform. Chen et al. studied a hybrid gait obstacle avoidance control strategy for a six-wheel-legged robot (BIT-6NAZA). It could ensure the horizontal stability of attitude by using a feedback controller when passing obstacles with different shapes [22]. The Ascento robot [23] was designed by ETH Zurich. The robot adopted the control strategy of the model-based linear quadratic regulator (LQR) to achieve balance and movement functions. It used a feedforward control strategy based on feedback tracking to perform jump and falling recovery functions. BIT developed the wheel-legged BHR-W robot [24] and proposed a layered controller. This hierarchical controller divided the controllers into a whole-body joint controller and a balanced motion controller to achieve the walking, jumping, roller-skating and other actions of the robot.

The reconfiguration of a deformable robot has been fast and global. Because of the speed of this reconfiguration, there has been a big impact on the robot. Therefore, it was necessary to analyse and design the smoothness of the reconfiguration process. Due to global reconfiguration, the shape, structure, degrees of freedom, position of the centre of mass and support domain have changed greatly during the reconfiguration process. Especially when the robot was reconstructed from the vehicle state to the humanoid state, the support domain would become significantly smaller. These factors would lead to the instability of the deformable robot during the reconfiguration process. It was necessary to analyse and improve the stability of this process.

In this paper, a new deformable robot was designed. The kinematic model of the reconfiguration of the deformable robot was established by using the homogeneous coordinate theory. On this basis, the joints turning angle motion laws were designed to improve the smoothness of the deformable robot during the reconfiguration process. The horizontal lifting motion model of the electric pusher and the lifting motor were established to ensure the levelness of the front body during the reconfiguration. According to the requirements of reconfiguration stability, the zero moment point (ZMP) theory was used to analyse the reconfiguration stability. The metamorphic mechanism was introduced to improve the stability of the deformable robot during the reconfiguration process. The research outlined above effectively improved the motion quality of the reconfiguration of the deformable robot.

2. Structure and reconfiguration planning of a deformable robot

Fig. 1 shows the three-dimensional model of the deformable robot in the vehicle state designed in this study. The four wheels on the front and rear bodies are electric wheels, which integrate hub motors, transmission, and braking devices. When the deformable robot is in the vehicle state, the leg mechanism is folded into the interior of the body. The robot has four-wheel drive (4WD), and also has the functions of steering, braking, and deceleration. To make the layout compact and reduce impact from the ground, McPherson suspension is used for both the front and the rear body.

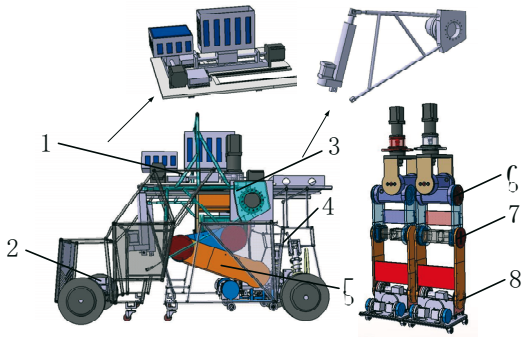

1. Metamorphic mechanism 2. Front body 3. Lifting mechanism 4. Rear body 5. Leg mechanism 6. Hip joint mechanism 7. Knee joint mechanism 8. Ankle joint mechanism.

Fig. 1 Three-dimensional model structure diagram of the deformable robot

The front and rear bodies are connected by a lifting mechanism, and the power sources of the lifting mechanism are a lifting motor and an electric pusher. The lifting motor is fixed on the rear body, and the V-shaped lifting rod is fixed on the output turntable of the lifting motor. The V-shaped lifting rod is composed of upper and lower lifting rods. The lower lifting rod is directly connected to the front body, and the upper lifting rod is indirectly connected to the front body through the electric pusher. To ensure the stability of the coupled reconfiguration process and the humanoid state when walking, a centre-of-mass position-adjusting mechanism was designed. This mechanism has a cruciform arrangement and is placed horizontally above the rear body. The slider of this mechanism can be controlled to move in a transverse and longitudinal direction to change the position of the centre of mass of the whole vehicle. To achieve a lightweight and space-saving design, batteries are used as the sliders.

The right-hand side of Fig. 1 shows a schematic diagram of the leg mechanism. It includes a hip joint mechanism, knee joint mechanism, and ankle joint mechanism. The hip joint mechanism can perform three-degree-of-freedom motion (yaw, roll, and pitch), the knee joint mechanism can achieve single-degree-of-freedom motion (pitch), and the ankle joint mechanism can achieve two-degree-of-freedom motion (pitch and roll). The leg mechanism is connected to the rear body through the base plate of the hip joint mechanism.

Under normal circumstances, the deformable robot runs on wheels in the vehicle state (as shown in Fig. 2(a)). When reconstructing, the legs will be expanded under the driving of the joint motors until the feet touch the ground. This state of the robot is called the support state (as shown in Fig. 2(b)). After this, the front body is lifted horizontally under the driving of the lifting motor and electric actuator, while the leg mechanism is further expanded until the vehicle stands up. The form at this time is called the humanoid state, as shown in Fig. 2(c).

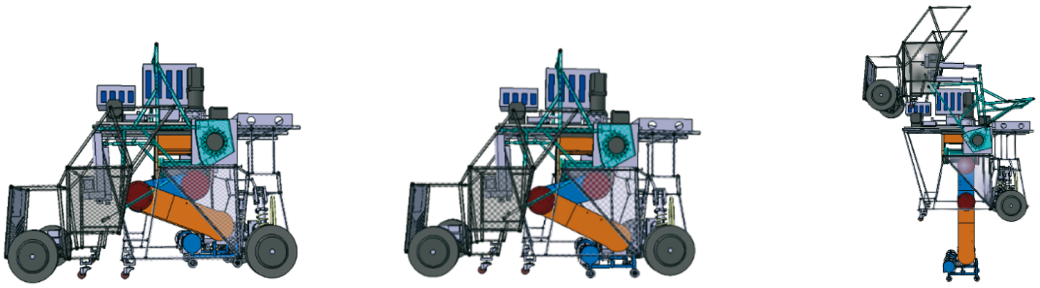

(a) Vehicle state of the deformable robot

(b) Support state of the deformable robot

(c) Humanoid state of the deformable robot

Fig. 2 Deformable robot configuration diagram

3. Kinematic modelling of the coupled reconfiguration and design of the motion target

3.1 Forward kinematic modelling

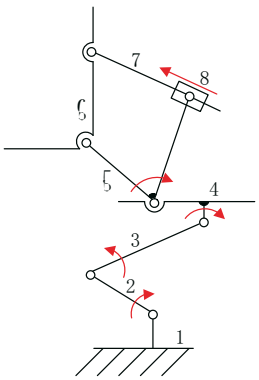

Fig. 3 Diagram of mechanism for the robot during the coupled reconfiguration process

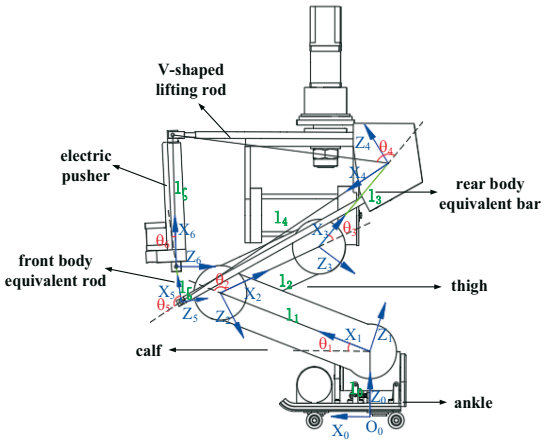

Fig. 4 Schematic diagram of the joint motion of the deformable robot

The two legs of the deformable robot designed in this study are bilaterally symmetric and have the same structure, so the mechanism on one side can be selected for analysis. In the process of coupled reconfiguration, the leg mechanism can be simplified to a serial RRR mechanism, and the lifting mechanism is simplified to a planar two-degree-of-freedom parallel RRRPR mechanism. The sketch of the mechanism is shown in Fig. 3, where the arrow points to the direction of movement of the prime mover.

The kinematic model of the deformable robot during the coupled reconfiguration process is established by applying the theory of homogeneous coordinate transformation [25-30]. The support state of the deformable robot is selected as the initial reference pose, and the base coordinate system $O_0 - X_0Y_0Z_0$, whose origin is the centre of the closed convex polygon support domain formed by two feet, is established on the ground where the supporting feet make contact. The X-axis of the base coordinate system points to the travel direction of the vehicle, the Y-axis points to the left of the travel direction of the vehicle, and the Z-axis is

perpendicular to the X-axis and points to the top of the robot. The coordinate system $O_1 - X_1Y_1Z_1$ of the calf is established at the ankle joint, and the X-axis points to the knee joint along the calf. The Y-axis and Z-axis both follow the right-hand rule of coordinate systems. Similarly, the coordinate systems of the thigh, the rear body equivalent rod, the upper lifting rod of the V-shaped lifting rod, and the front body equivalent rod are established at the articulation points of the knee joint, the hip joint, the lift joint, the lower lifting rod of the V-shaped lifting rod, and the front body, respectively. The schematic diagram of the joint motion of the deformable robot is shown in Fig. 4. In the figure, θ_i $(i = 1\text{–}6)$ indicates the rotation angle of each component, and l_i $(i = 0\text{–}6)$ indicates the length of each component.

The homogeneous transformation matrix of the adjacent coordinate systems are as follows.

The coordinate system of the calf relative to the basic coordinate system is

$$ {}^{0}_{1}\boldsymbol{T} = \begin{pmatrix} \cos\theta_1 & 0 & -\sin\theta_1 & 0 \\ 0 & 1 & 0 & 0 \\ \sin\theta_1 & 0 & \cos\theta_1 & l_0 \\ 0 & 0 & 0 & 1 \end{pmatrix}. \tag{1} $$

In addition, the homogeneous transformation matrix between other adjacent coordinate systems (the coordinate system of the thigh relative to the coordinate system of the calf, the coordinate system of the rear body equivalent rod relative to the coordinate system of the thigh, the lower rod coordinate system of the V-shaped lifting rod relative to the coordinate system of the rear body equivalent rod, the coordinate system of the front body equivalent rod relative to the lower rod coordinate system of the V-shaped lifting rod) can be expressed successively as ${}^{i-1}_{i}\boldsymbol{T}(i = 2\sim5)$:

$$ {}^{i-1}_{i}\boldsymbol{T} = \begin{pmatrix} \cos\theta_i & 0 & -\sin\theta_i & l_{i-1} \\ 0 & 1 & 0 & 0 \\ \sin\theta_i & 0 & \cos\theta_i & 0 \\ 0 & 0 & 0 & 1 \end{pmatrix}. \tag{2} $$

From Eqs (1) to (2), the homogeneous transformation matrices of the coordinate system of each component relative to the base coordinate system can be obtained, as follows:

$$ {}^{0}_{i}\boldsymbol{T} = {}^{0}_{1}\boldsymbol{T} \times \cdots \times {}^{\mathrm{i}-1}_{\mathrm{i}}\boldsymbol{T}\ (i = 2\text{–}5). \tag{3} $$

When the values of i are from 2 to 5, the homogeneous transformation matrices of the thigh coordinate system, the rear body equivalent rod coordinate system, the lower rod coordinate system of the V-shaped lifting rod, and the front body equivalent rod coordinate system can be obtained in turn.

To facilitate the establishment of the model, the centre of mass of the calf, thigh, and lower rod of the V-shaped lifting rod is considered to be at the geometric centre of the rod (the centre of mass of the rod is at the midpoint of the rod), and the position vector of the centre of mass c_i of each rod in the basic coordinate system can be obtained as follows.

The centre of mass of the calf:

$$ \boldsymbol{C}_1 = \left(\frac{l_1c_1}{2}, 0, \frac{l_1s_1}{2} + l_0\right)^T. \tag{4} $$

The centre of mass of the thigh:

$$ \boldsymbol{C}_2 = \left(\frac{l_2c_2}{2} + l_1c_1, 0, \frac{l_2s_2}{2} + l_1c_1 + l_0\right)^T. \tag{5} $$

The centre of mass of the lower rod of the V-shaped lifting rod:

$$\boldsymbol{C}_3 = \begin{pmatrix} \frac{l_4 c_4}{2} + l_2 c_2 + l_1 c_1 + l_3 c_3 \\ 0 \\ l_0 + \frac{l_4 s_4}{2} + l_2 s_2 + l_1 s_1 + l_3 s_3 \end{pmatrix}^T. \tag{6}$$

The centre of mass of the upper rod of the V-shaped lifting rod:

$$\boldsymbol{C}_4 = \begin{pmatrix} \frac{l_7 c_\lambda}{2} + l_2 c_2 + l_1 c_1 + l_3 c_3 \\ 0 \\ l_0 + \frac{l_7 s_\lambda}{2} + l_2 s_2 + l_1 s_1 + l_3 s_3 \end{pmatrix}^T. \tag{7}$$

The position vector of the centre of mass of the rear body in the coordinate system $O_3 - X_3 Y_3 Z_3$ is $c_r = [x_r, 0, z_r]^T$, so the centre of mass of the rear body is as follows:

$$\boldsymbol{C}_r = \begin{pmatrix} l_2 c_2 + l_1 c_1 + x_r c_3 - z_r s_3 \\ 0 \\ z_r c_3 + x_r s_3 + l_2 s_2 + l_1 s_1 + l_0 \end{pmatrix}. \tag{8}$$

The position vector of the centre of mass of the front body (end mechanism of the system) in the coordinate system $O_5 - X_5 Y_5 Z_5$ is $c_r = [x_r, 0, z_r]^T$, so the centre of mass of the front body is as follows:

$$\boldsymbol{C}_f = \begin{pmatrix} l_4 c_4 + l_2 c_2 + l_1 c_1 + l_3 c_3 + x_f c_5 - z_f s_5 \\ 0 \\ l_0 + l_4 s_4 + l_2 s_2 + l_1 s_1 + z_f c_5 + l_3 s_3 + x_f s_5 \end{pmatrix}. \tag{9}$$

Because both ends of the electric pusher are connected to the upper rod of the V-shaped lifting rod and the front body equivalent rod, respectively, the position vectors of both ends of the electric pusher can be solved by the homogeneous transformation matrix.

The position vector of the lower connection endpoint of the electric pusher is as follows:

$$\begin{pmatrix} l_1 c_1 + l_2 c_2 + l_3 c_3 + l_4 c_4 + l_5 c_5 \\ 0 \\ l_0 + l_1 s_1 + l_2 s_2 + l_3 s_3 + l_4 s_4 + l_5 s_5 \\ 1 \end{pmatrix}. \tag{10}$$

The position vector of the upper connection endpoint of the electric pusher is:

$$\begin{pmatrix} l_1 c_1 + l_2 c_2 + l_3 c_3 + l_7 c_\lambda \\ 0 \\ l_0 + l_1 s_1 + l_2 s_2 + l_3 s_3 + l_7 s_\lambda \\ 1 \end{pmatrix}. \tag{11}$$

The centre of mass of the electric pusher by Eqs (10)–(11) is:

$$\boldsymbol{C}_5 = \begin{pmatrix} l_1 c_1 + l_2 c_2 + l_3 c_3 + \frac{l_4 c_4 + l_5 c_5 + l_7 c_\lambda}{2} \\ 0 \\ l_0 + l_1 s_1 + l_2 s_2 + l_3 s_3 + \frac{l_4 s_4 + l_5 s_5 + l_7 s_\lambda}{2} \end{pmatrix}. \tag{12}$$

The angle between the trajectory line of the lower rear body slider mass and the line connecting the hip joint and the lift joint at the rear body is a constant value η. Therefore, the position vector of the centre-of-mass position-adjusting mechanism in the coordinate system

$O_3 - X_3Y_3Z_3$ is $[\cos\eta \cdot sl, 0, -\sin\eta \cdot sl]^T$, where sl represents the displacement of the slider. The centre of mass of the metamorphic core slider mechanism is as follows:

$$\boldsymbol{C}_b = \begin{pmatrix} l_1c_1 + l_2c_2 + \sin\eta \cdot sl \cdot s_3 + \cos\eta \cdot sl \cdot c_3 \\ 0 \\ l_0 + l_1s_1 + l_2s_2 - \sin\eta \cdot sl \cdot c_3 + \cos\eta \cdot sl \cdot s_3 \end{pmatrix}. \tag{13}$$

Based on Eqs (4)–(12) and (13), it is known that the position vector of the centre of mass of the vehicle in the basic coordinate systems during the coupled reconfiguration process is as follows:

$$\boldsymbol{C} = (\boldsymbol{C}_1m_1 + \boldsymbol{C}_2m_2 + \boldsymbol{C}_\mathrm{r}m_3 + \boldsymbol{C}_\mathrm{f}m_5 + \boldsymbol{C}_3m_4 + \boldsymbol{C}_4m_7 + \boldsymbol{C}_5m_6$$

$$+\boldsymbol{C}_\mathrm{b}m_b) \,/\, (m_1 + m_2 + m_3 + m_4 + m_5 + m_6 + m_7 + m_b), \tag{14}$$

where $s_1 = \sin(\theta_1)$, $s_2 = \sin(\theta_1 + \theta_2)$, $s_3 = \sin(\theta_1 + \theta_2 + \theta_3)$, $s_4 = \sin(\theta_1 + \theta_2 + \theta_3 + \theta_4)$, $s_5 = \sin(\theta_1 + \theta_2 + \theta_3 + \theta_4 + \theta_5)$, $s_\lambda = \sin(\theta_1 + \theta_2 + \theta_3 + \theta_4 + \theta_\lambda)$, $c_1 = \cos(\theta_1)$, $c_2 = \cos(\theta_1 + \theta_2)$, $c_3 = \cos(\theta_1 + \theta_2 + \theta_3)$, $c_4 = \cos(\theta_1 + \theta_2 + \theta_3 + \theta_4)$, $c_5 = \cos(\theta_1 + \theta_2 + \theta_3 + \theta_4 + \theta_5)$, $c_\lambda = \cos(\theta_1 + \theta_2 + \theta_3 + \theta_4 + \theta_\lambda)$.

3.2 Horizontal lifting motion design

To meet the horizontal lifting requirements, the front and rear bodies must always remain horizontal. During the coupled reconfiguration process, the rotation angles of each joint to maintain the rear body level meet the following requirement:

$$\theta_1 + \theta_2 + \theta_3 = \frac{13}{18}\pi. \tag{15}$$

The horizontal state of the front body is ensured by the electric pusher and lifting motor. When the lifting joint angle θ_4 becomes larger, the front body will rotate counter clockwise, and in this time the electric pusher extends to push the front body to the horizontal position. Therefore, the relationship between the stroke S of the electric pusher and the rotation angle θ_4 of the lifting joint can be deduced.

First, the change of the electric pusher stroke S will cause a change of θ_5, where θ_5 is the angle between the upper rod of the V-shaped lifting rod and the front body equivalent rod. The homogeneous transformation matrix of the point where the electric pusher is connected with the front body equivalent rod in the coordinate system $O_4 - X_4Y_4Z_4$ is expressed as follows:

$${}^4_5\boldsymbol{T}\begin{pmatrix} l_5 \\ 0 \\ 0 \\ 1 \end{pmatrix} = \begin{pmatrix} \cos\theta_5 & 0 & -\sin\theta_5 & l_4 \\ 0 & 1 & 0 & 0 \\ \sin\theta_5 & 0 & \cos\theta_5 & 0 \\ 0 & 0 & 0 & 1 \end{pmatrix}\begin{pmatrix} l_5 \\ 0 \\ 0 \\ 1 \end{pmatrix} = \begin{pmatrix} l_4 + l_5\cos\theta_5 \\ 0 \\ l_5\sin\theta_5 \\ 1 \end{pmatrix}. \tag{16}$$

The homogeneous transformation matrix of the point where the electric pusher is connected with the upper rod of the V-shaped lifting rod in the coordinate system $O_4 - X_4Y_4Z_4$ is expressed as follows:

$$\begin{pmatrix} \cos\lambda & 0 & -\sin\lambda & 0 \\ 0 & 1 & 0 & 0 \\ \sin\lambda & 0 & \cos\lambda & 0 \\ 0 & 0 & 0 & 1 \end{pmatrix}\begin{pmatrix} l_7 \\ 0 \\ 0 \\ 1 \end{pmatrix} = \begin{pmatrix} l_7\cos\lambda \\ 0 \\ l_7\sin\lambda \\ 1 \end{pmatrix}. \tag{17}$$

Using the space distance formula between two points, the total length $l_6 + S$ of the electric pusher during the front body lifting process can be written as follows:

$$l_6 + S = \sqrt{(l_4 + l_5\cos\theta_5 - l_7\cos\lambda)^2 + (l_5\sin\theta_5 - l_7\sin\lambda)^2}. \tag{18}$$

Second, since the front body is kept in a horizontal position during the lifting process, the relationship between θ_5 and the lifting joint angle θ_4 is as follows:

$$\theta_5 = \alpha + \beta - (\theta_4 - \theta_{40}). \tag{19}$$

Fig. 5 shows the schematic diagram of the lifting mechanism, where λ is the angle between the upper and lower rods of the V-shaped lifting rod and is a constant value, l_7 is the length of the upper rod of the V-shaped lifting rod, α is the angle between the lower rod of the V-shaped lifting rod and the horizontal line, θ_{40} is the initial angle of θ_4, and β is the angle between the front body equivalent rod and the horizontal line. Eqs (18) and (19) show that if the front body needs to remain level during the lifting process, the relationship between the stroke S of the electric pusher and the rotation angle θ_4 of the lifting joint should be as follows:

$$\begin{cases} l_6 + S == \sqrt{(l_4 + l_5\cos\theta_5 - l_7\cos\lambda)^2 + (l_5\sin\theta_5 - l_7\sin\lambda)^2} \\ \theta_5 = \alpha + \beta - (\theta_4 - \theta_{40}) \end{cases}. \tag{20}$$

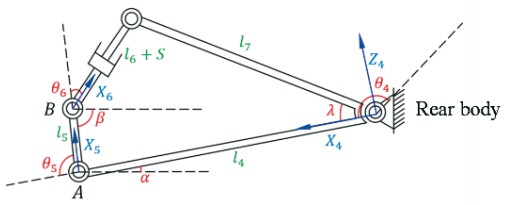

Fig. 5 Structural diagram of the lifting mechanism

3.3 Motion smoothness design for coupled reconfiguration processes

During the coupled reconfiguration process, to avoid impact damage to the vehicle and on-board equipment, the motion of each joint should meet smoothness and rapidity requirements. Therefore, the motion law of the joint motor should restrict the position and the velocity and acceleration. The angular displacement model θ_i $(i = 1\text{–}5)$ of the rotating joint with time *t* is chosen as a fifth-order polynomial [31]:

$$\theta_i = a_0 + a_1 t + a_2 t^2 + a_3 t^3 + a_4 t^4 + a_5 t^5. \tag{21}$$

In the case of the deformable robot, the operation process has the following requirements:

1) no abrupt changes in velocity and acceleration can occur at the start and end times of the operation of each rotating joint;
2) the coupled reconfiguration must be completed within a specified time τ.

Accordingly, the following boundary conditions can be derived:

$$\begin{cases} \theta_i(0) = 0 \\ \theta_i(\tau) = \Delta\theta_i \\ \dot{\theta}_i(0) = 0 \\ \dot{\theta}_i(\tau) = 0 \\ \ddot{\theta}_i(0) = 0 \\ \ddot{\theta}_i(\tau) = 0 \end{cases}, \tag{22}$$

where θ_i is the angle of each rotating joint, $\dot{\theta}_i$ is the angular velocity of each rotating joint, $\ddot{\theta}_i$ is the angular acceleration of each rotating joint, and $\Delta\theta_i$ is the turned angle of each rotating joint within the reconfiguration time τ.

By substituting Eq (21) into Eq (22), the following can be obtained:

$$\begin{cases} \theta_i(0) = a_0 = 0 \\ \theta_i(\tau) = a_0 + a_1\tau + a_2\tau^2 + a_3\tau^3 + a_4\tau^4 + a_5\tau^5 = \Delta\theta_i \\ \dot{\theta}_i(0) = a_1 = 0 \\ \dot{\theta}_i(\tau) = a_1 + 2a_2\tau + 3a_3\tau^2 + 4a_4\tau^3 + 5a_5\tau^4 = 0 \\ \ddot{\theta}_i(0) = 2a_2 = 0 \\ \ddot{\theta}_i(\tau) = 2a_2 + 6a_3\tau + 12a_4\tau^2 + 20a_5\tau^3 = 0 \end{cases}. \tag{23}$$

The values of $a_0 - a_5$ can be obtained as follows:

$$(a_0 \quad a_1 \quad a_2 \quad a_3 \quad a_4 \quad a_5)^T = \left(0 \quad 0 \quad 0 \quad \frac{10\Delta\theta_i}{\tau^3} \quad -\frac{15\Delta\theta_i}{\tau^4} \quad \frac{6\Delta\theta_i}{\tau^5}\right)^T. \tag{24}$$

By substituting Eq (24) into Eq (21), we obtain the angular displacement motion equation of the rotating joint:

$$\theta_i = \frac{10\Delta\theta_i}{\tau^3}t^3 - \frac{15\Delta\theta_i}{\tau^4}t^4 + \frac{6\Delta\theta_i}{\tau^5}t^5. \tag{25}$$

The angular velocity motion equation of the rotating joint can be obtained by taking the first derivative with respect to *t*:

$$\dot{\theta}_i = \frac{30\Delta\theta_i}{\tau^3}t^2 - \frac{60\Delta\theta_i}{\tau^4}t^3 + \frac{30\Delta\theta_i}{\tau^5}t^4. \tag{26}$$

The angular acceleration motion equation of the rotating joint can be obtained by taking the second derivative with respect to *t*:

$$\ddot{\theta}_i = \frac{60\Delta\theta_i}{\tau^3}t - \frac{180\Delta\theta_i}{\tau^4}t^2 + \frac{120\Delta\theta_i}{\tau^5}t^3. \tag{27}$$

The angular jerk motion equation of the rotating joint can be obtained by taking the third derivative with respect to *t*:

$$\dddot{\theta}_{\mathrm{i}} = \frac{60\Delta\theta_i}{\tau^3} - \frac{360\Delta\theta_i}{\tau^4}t + \frac{360\Delta\theta_i}{\tau^5}t^2. \tag{28}$$

Equation (28) is a quadratic function, and the curve is smooth, which means that when the joint motor is rotating according to Eq (25), the whole reconfiguration motion process, including the start and end of the reconfiguration, will be smooth and without impact.

Based on the results in Sections 3.2 and 3.3, the rotation angles of each joint of the deformable robot during the coupled reconfiguration should satisfy the following conditions:

$$\begin{cases} l_6 + S = \sqrt{(l_4 + l_5\cos\theta_5 - l_7\cos\lambda)^2 + (l_5\sin\theta_5 - l_7\sin\lambda)^2} \\ \theta_5 = \alpha + \beta - (\theta_4 - \theta_{40}) \\ \theta_1 + \theta_2 + \theta_3 = \frac{13}{18}\pi \\ \theta_i = \frac{10\Delta\theta_i}{\tau^3}t^3 - \frac{15\Delta\theta_i}{\tau^4}t^4 + \frac{6\Delta\theta_i}{\tau^5}t^5 \end{cases}. \tag{29}$$

3.4 Reconfiguration stability criterion of the deformable robot

The deformable robot undergoes global reconfiguration during wheel-leg switching. The global nature of the reconfiguration is mainly reflected in significant changes before and after the reconfiguration. In the case of global reconfiguration, stability should be considered, and it is also an important index to evaluate the motion quality of the coupled reconfiguration.

Reconfiguration motion is a complex, spatially coupled motion. In the process of reconfiguration, each component of the robot is affected by gravity, driving forces, friction, and inertial forces. In this study, the ZMP method was chosen as the criterion to judge stability. The ZMP is a point on the ground [32], which is the intersection of the resultant direction of the whole mechanism and the ground.

Assuming that the mass of each component of the deformable robot is m_i and the coordinates of the centre of mass of each component are (x_i, y_i, z_i), the expression of ZMP can be deduced by the d'Alembert principle as follows:

$$x_{ZMP} = \frac{\sum_{i=1}^{n} m_i(\ddot{z}_i+g)x_i - \sum_{i=1}^{n} m_i\ddot{x}_i z_i}{\sum_{i=1}^{n} m_i(\ddot{z}_i+g)}, \tag{30}$$

$$y_{ZMP} = \frac{\sum_{i=1}^{n} m_i(\ddot{z}_i+g)y_i - \sum_{i=1}^{n} m_i\ddot{y}_i z_i}{\sum_{i=1}^{n} m_i(\ddot{z}_i+g)}, \tag{31}$$

where g is the acceleration of gravity, m_i is the mass of each component i, x_i , y_i, and z_i are the coordinate values of the centre of mass of each component in the directions of the x, y and z coordinate axes, respectively, and $\ddot{x}_i$, $\ddot{y}_i$, and $\ddot{z}_i$ are the acceleration of the centre of mass of each component in the directions of the x, y, and z coordinate axes, respectively.

4. Simulation analysis of the coupled reconfiguration motion

According to the design results in Section 3, the coupled reconfiguration motion of the deformable robot is simulated by Matlab/Simulink. The smoothness of the reconfiguration motion, the accuracy of the horizontal design, and the effectiveness of the metamorphic mechanism to regulate the reconfiguration stability are verified.

4.1 Motion smoothness and horizontality simulation during the coupled reconfiguration of the deformable robot

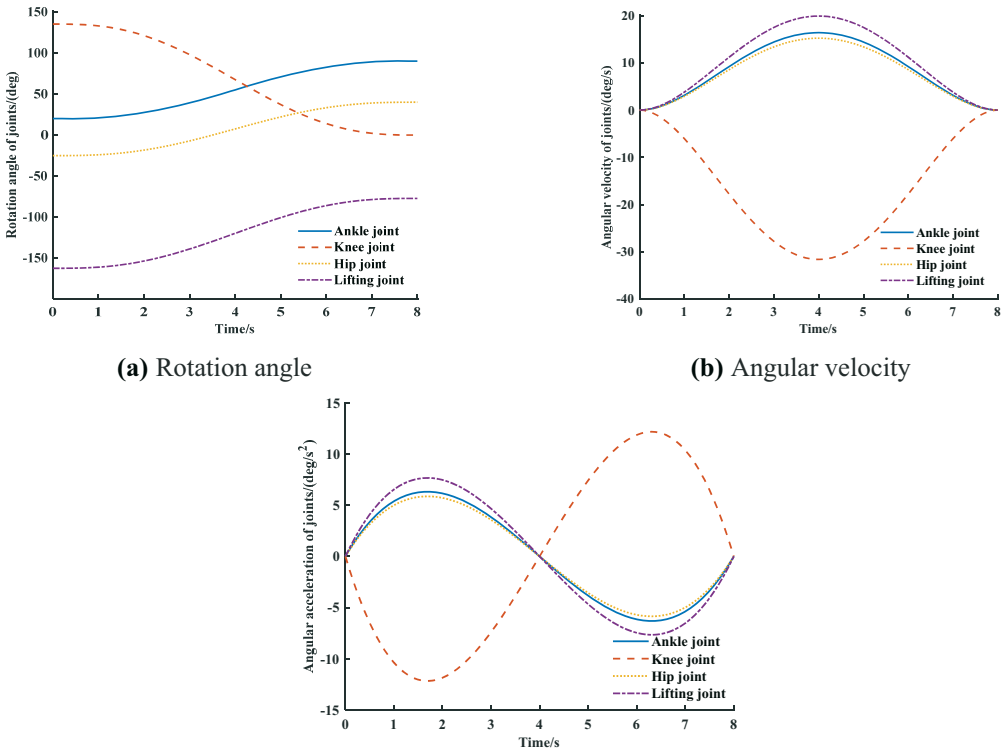

(a) Rotation angle

(b) Angular velocity

(c) Angular acceleration

Fig. 6 Diagram of each joint movement

With the support state in Fig. 2(b) as the starting state, the deformable robot completed the coupled reconfiguration from the support state to the humanoid state within $\tau = 8$ s according to the reconfiguration planning. The initial angle, final angle, and rotation angle of each joint are shown in Table 1.

Table 1 Parameters for each joint motion

Joint motor angle (deg)	Simulation time (s)	Initial angle (deg)	Angle range (deg)	Final angle (deg)
Ankle joint $\boldsymbol{\theta_1}$	8	20	70	90
Knee joint $\boldsymbol{\theta_2}$	8	135	−135	0
Hip joint $\boldsymbol{\theta_3}$	8	−25	65	40
Lifting joint $\boldsymbol{\theta_4}$	8	−162	85	−77

Fig. 6 shows the motion of each joint. During the coupled reconfiguration process, the rotation angular velocities of the lifting joint, hip joint, knee joint, and ankle joint were nonlinear and unequal. The angular velocity and the angular acceleration of each joint were zero at the start and end of the coupled reconfiguration, and the angular velocity and acceleration of each joint motor changed smoothly and continuously during the coupled reconfiguration process, which was mainly to avoid the impact and shock of the system, thus satisfying the design requirements of smoothness.

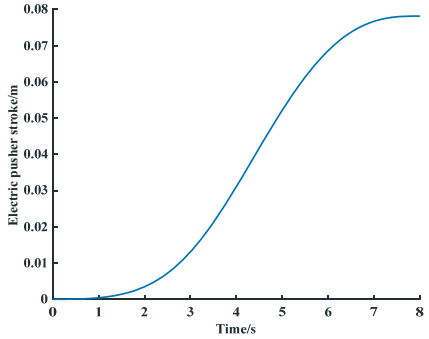

Fig. 7 Electric push rod stroke diagram

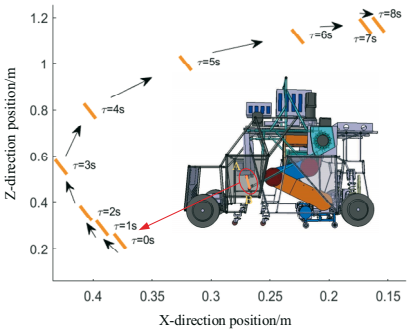

Fig. 8 Trajectory of the front body equivalent rod in the XZ-plane

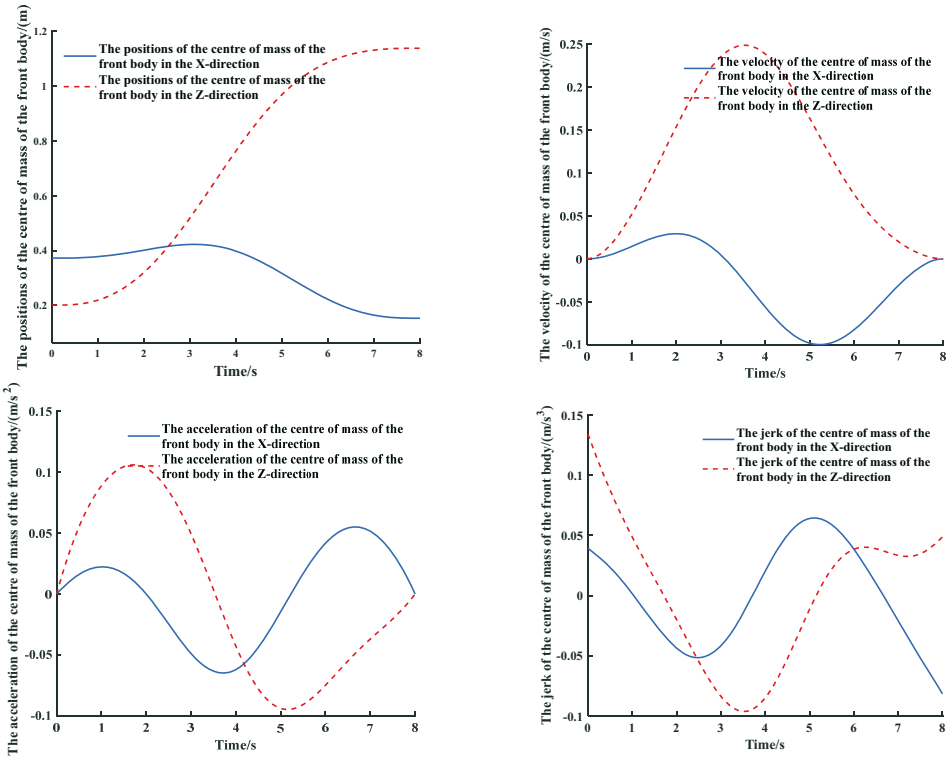

Fig. 9 Variation of the centre of mass of the front body

Fig. 7 shows the variation of the electric pusher stroke S. The electric pusher extended 0.072 m during the coupled reconfiguration process, and the curve was continuous and smooth. The second derivative of this stroke showed that the linear acceleration at the beginning and end of the phase was zero. Fig. 8 shows the motion trajectory of the front body equivalent rod. The angle between the front body equivalent rod and the horizontal line always remained unchanged, and thus the front body could always stay horizontal under the action of the electric pusher, which proved the correctness of the established horizontal lifting model.

As shown in Figs. 9 and 10, when each active joint operated with the fifth-order polynomial function, the front body and the whole vehicle ran smoothly during the coupled reconfiguration process. The positions of the centre of mass of the front body and the whole vehicle increased in the Z-direction during the coupled reconfiguration, while the values in the X-direction were consistently less, and the centre of mass shifted backward. Furthermore, the differences between the maximum and minimum of the velocity, acceleration, and jerk of the centre of mass of the front body and the whole vehicle in the X-direction were less than those in the Z-direction, respectively.

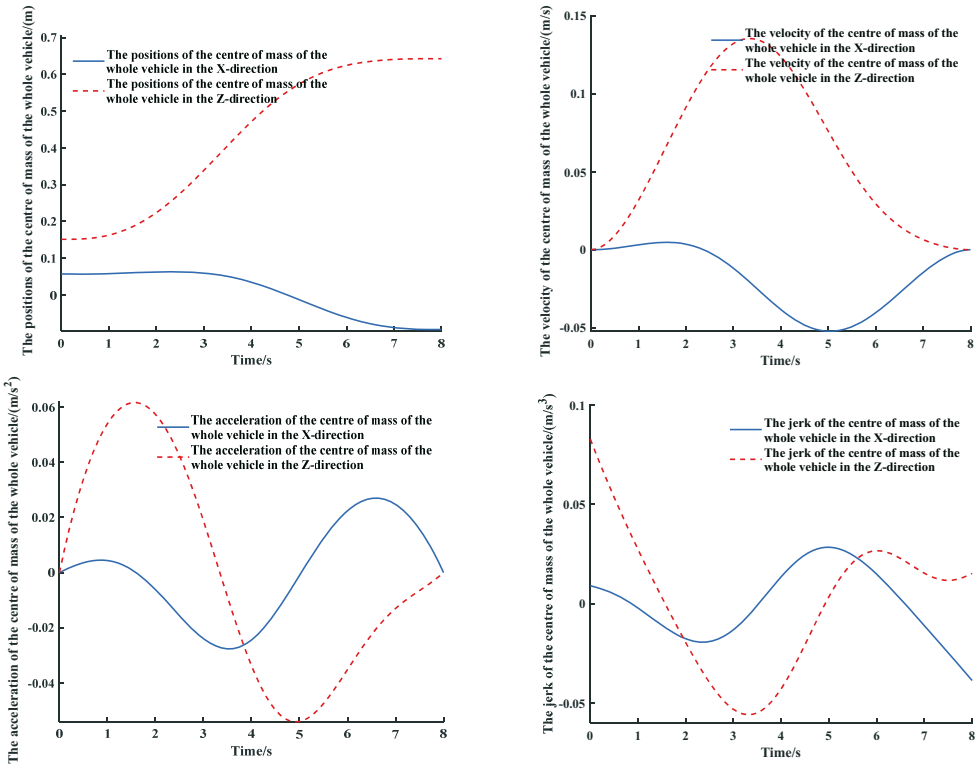

Fig. 10 Variation of the centre of mass of the whole vehicle

4.2 Motion stability simulation during the coupled reconfiguration of the deformable robot

In this paper, the support domain of the deformable robot is expressed as follows:

$$s = \begin{cases} -0.086 < x < 0.086 \\ -0.17 < y < 0.17 \end{cases} (0 \le t \le 8). \tag{32}$$

Since the instability of the deformable robot during the coupled reconfiguration process mainly manifested as tilting in the X-direction, only the change of the ZMP in the X-direction is considered here. First, without considering the influence of the slider, the variation curve of the ZMP in the X-direction can be obtained, as shown in Fig. 11(a).

Table 2 Comparison of the stability margins under three working conditions

Stability margin(m)	Maximum value	Minimum value	Average value
No slider	0.086	-0.019	0.041
Slider at rest	0.086	0.011	0.037
Slider movement	0.086	0.041	0.068

During the 8-s coupled reconfiguration, the ZMP of the deformable robot was 0.038 m at the initial time, and then the ZMP kept moving in the negative X-direction as the coupled reconfiguration continued. At 6.3 s, the ZMP of the deformable robot exceeded the support domain, then the stability margin (defined as the distance between the ZMP and the near boundary of the support domain) crossed 0 and gradually became more negative, as shown in Table 2. The minimum stability margin was −0.019 m, indicating that the mechanism had become unstable at this time.

To maintain stability at all times during the coupled reconfiguration process, a controllable centre-of-mass position-adjusting mechanism was installed on the base plate of the deformable robot. The position of the centre of mass of the deformable robot during the coupled reconfiguration process can be changed by sliding two sliders (batteries) back and forth in the X-direction, or left and right in the Y-direction. When the centre of mass of the slider remained at the initial state position (SL = 0), the change of ZMP is shown in Fig. 11(b).

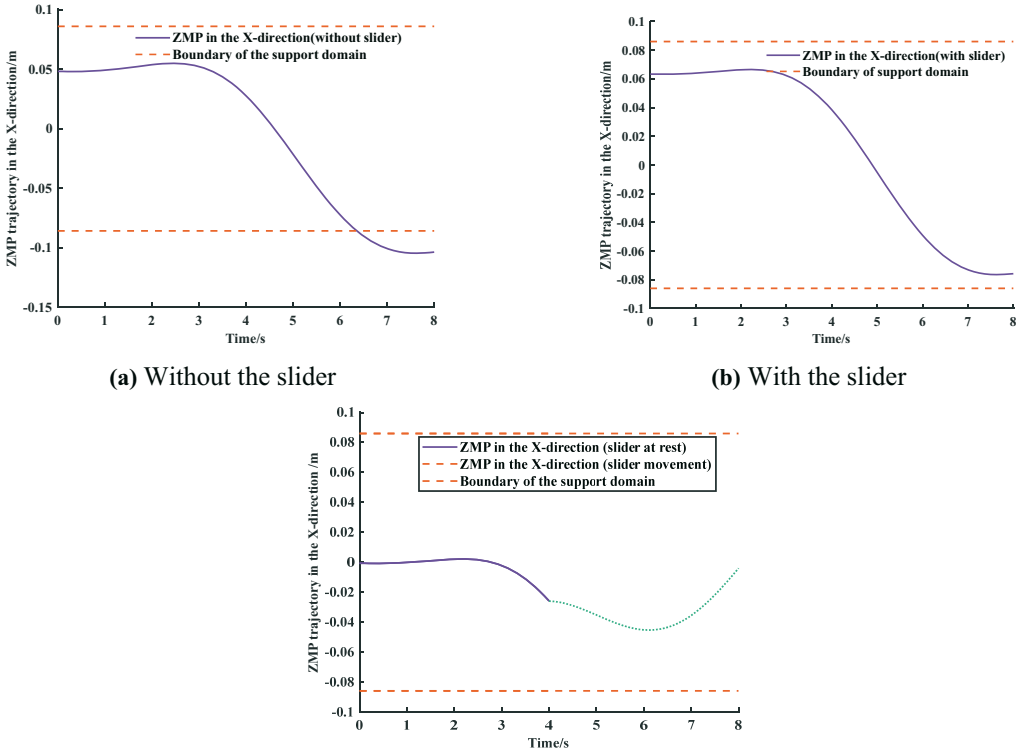

(a) Without the slider

(b) With the slider

(c) Under the movement of the slider

Fig. 11 X_{ZMP} curve of the whole vehicle under different conditions

During the 8-s coupled reconfiguration, the initial stability margin in the X-direction was 0.023 m. After that, the ZMP of the whole system kept moving toward the rear of the robot. When it reached 8 s, as shown in Fig. 11(b) and Table 2, the minimum stability margin of the whole system reached 0.011 m. Throughout the coupled reconfiguration process, the ZMP was in the support domain, which indicated the stability of the deformable robot during the coupled reconfiguration process. In addition, it can be seen that at the beginning and end of the coupled

process, the deformable robot was close to the unstable state. Therefore, the following motion was designed for the slider in the subsequent research:

$$sl = \begin{cases} -0.1(t < 4s) \\ 0.1t - 0.5(4s < t < 8s) \end{cases}. \tag{33}$$

As shown in Fig. 11(c), the ZMP was optimized when the slider was controlled to move according to Eq (33). First, the ZMP was at the centre of the support domain at the start time. The variation of the ZMP showed that the stability margin always maintained a large value during the whole coupled reconfiguration, and the curve reached the minimum value of 0.041 at 6.2 s. As shown in Table 2, the minimum stability margin and the average stability margin were larger than those without the slider or with the stationary slider, which indicated that the reconfiguration stability of the deformable robot was significantly improved.

5. Prototype experiments of the coupled reconfiguration motion

5.1 Construction of the experimental platform

The experimental platform was mainly composed of a prototype of the deformable robot and a measurement and control system. As shown in Fig. 12, the prototype of the deformable robot included two legs, a front body, a rear body, a lifting mechanism, and a centre-of-mass position-adjusting mechanism. The measurement and control system consisted of an upper computer (PC), a lower computer for the controller (ECU), sensors (inertial measurement unit (IMU), force sensing resistor (FSR), electrical actuators (joint stepper motor, lifting motor, electric pusher, control motor of the slider), and a robot power supply. The upper computer was used as the human–machine interface. It was used to run the LabVIEW software, set the operation control parameters of the motors and other actuators, and display the movement information of the deformable robot. The lower computer mainly received digital signals from each sensor and performed the control of the underlying actuator. The communication between the upper computer and the lower computer was achieved through the serial port. Fig. 13 shows the schematic diagram of the control system of the deformable robot.

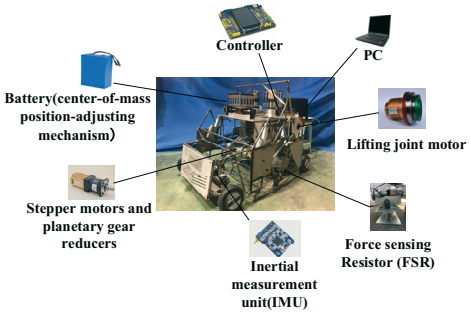

Fig. 12 Deformable robot prototype

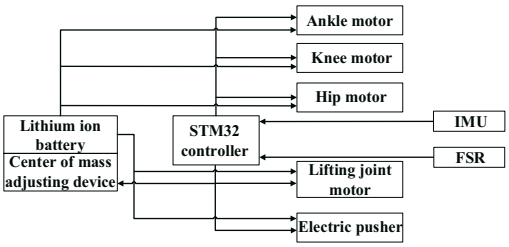

Fig. 13 Schematic diagram of the control system

The IMU used an MPU6050 gyroscope module which could be used to measure the changes of the centre of mass and pitch angle of the front body if mounted at the absolute centre of mass of the front body. The FSRs were installed at four symmetric positions of the left front, right front, left rear, and right rear of the sole to measure the pressure change of the CoP (centre of pressure on the sole). For a deformable robot under dynamic balance, its feet are always in a supporting state with the ground, and the ZMP is coincident with the CoP according to the theory previously reported [33]. Therefore, the FSR could be used to detect the pressure changes of the plantar during the coupled reconfiguration process in real time, and the value of the ZMP could be obtained according to the calculation of the CoP [34].

5.2 Experimental verification of the motion qualities of the deformable robot during coupled reconfiguration

The motion of the electric pusher and rotation motor given by Eq. (33) was programmed into the controller to control the operation of each active component. The experimental process of the coupled reconfiguration is shown in Fig. 14, where ① is the support state and ④ is the humanoid state.

The pitch angle measured by the IMU in the experiments was used as the evaluation index to judge whether the front body was horizontal, as shown in Fig. 15.

There was a small change in the pitch angle when the coupled reconfiguration started and stopped, which was caused by the inertia of the body. The maximum range of the change did not exceed 1.6°, and the reason for the change in the pitch angle of the front body was the jitter caused by the elasticity of the lifting rod. However, the error variation was within a reasonable range, which confirmed the effectiveness of the horizontal lifting model of the front body established in Section 3.2. Meanwhile, closed-loop feedback control will be added to the motor control in a subsequent study to reduce the elastic vibrations caused by the rod.

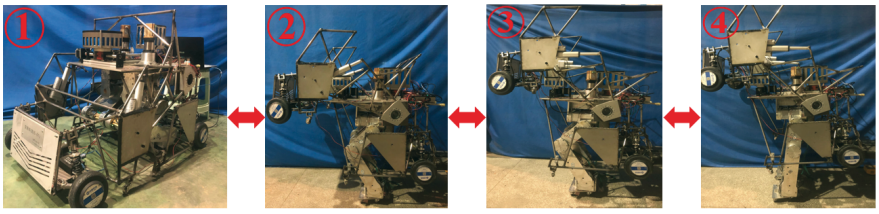

Fig. 14 Sequence diagram for the coupled reconfiguration of the deformable robot

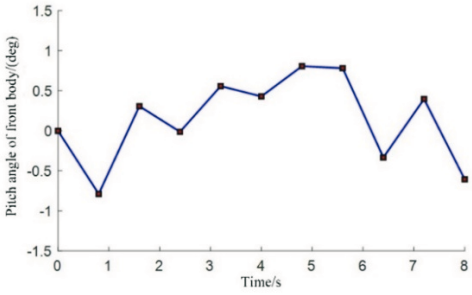

Fig. 15 Pitch angle curve of the front body

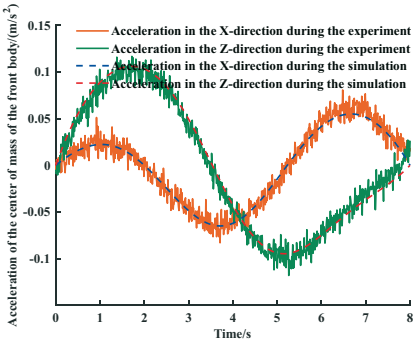

Fig. 16 Acceleration of the centre of mass of the front body from the simulation and experiment

The acceleration of the centre of mass of the front body in the X- and Z-directions could also be measured by the IMU, which was used as the evaluation index of the coupled reconfiguration smoothness design, as shown in Fig. 16. The acceleration of the centre of mass of the front body in the X- and Z-directions changed stably with time during the coupled reconfiguration process, and the curve measured by the experiments was basically consistent with the trend of the simulation curve. Based on the mean square error (MSE) formula, the deviation between the real and simulated values was quantified. The MSE in the X-direction was $\mathrm{MSE_{fax}} = 5.23 \times 10^{-5}$, and the mean square error in the Z-direction was $\mathrm{MSE_{faz}} = 1.42 \times 10^{-4}$, both of which were very small and close to zero. This showed the accuracy of the kinematics model established above.

As shown in Fig. 16, the acceleration of the centre of mass of the front body in the positive X-direction increased gradually from 0.002 m/s^2 at the beginning and reached a maximum value of 0.051 m/s^2 at 0.9 s. It then decreased to 0 m/s^2 at 2 s, increased in the negative X-direction to a maximum of 0.083 m/s^2 at 3.7 s, decreased to 0 m/s^2 at 5.5 s, and increased to a positive

maximum value of 0.081 m/s^2 at 6.4 s. Finally, it steadily decreased to 0.019 m/s^2 at the end of the reconfiguration. Similarly, the acceleration of the centre of mass of the front body in the positive Z-direction first increased from 0.009 m/s2 to a maximum of 0.117 m/s^2 from 0 to 1.6 s, then it decreased to 0 m/s^2 at 3.5 s, and then increased in the negative Z-direction and reached a maximum of 0.118 m/s^2 at 5 s. At the end of the reconfiguration, it steadily decreased to 0.026 m/s^2. The acceleration variation showed that the angular displacement model of the rotating joint could make the joint rotate with high flexibility, which allowed the front body to run smoothly without impact during the coupled reconfiguration process. The measured value of the acceleration exhibited a jittering phenomenon, which was caused by the zero drift and noise interference of the sensor itself.

In the stability test of the coupled reconfiguration, for safety reasons (the deformable robot could collapse when the leg was at the edge of the support domain), only an experiment under the movement rule of the slider given by Eq. (33) (the slider moved in the X-direction) was conducted, as shown in Fig. 17.

As shown in Fig. 18, the variation trend of the CoP curve was consistent with that of the ZMP curve, and the CoP always remained in the stable region during the coupled reconfiguration process. The deformable robot ran smoothly and did not tip over during the test. This result was also consistent with the simulation conclusion that the coupled reconfiguration process of the deformable robot remained stable. There was a certain error between the CoP curve and the expected curve of the ZMP. This error was small, and the reason was mainly due to the differences between the theoretical mathematical model and the robot prototype structure. The CoP curve underwent small oscillations, which were caused by the noise interference of the sensor, which is a normal phenomenon.

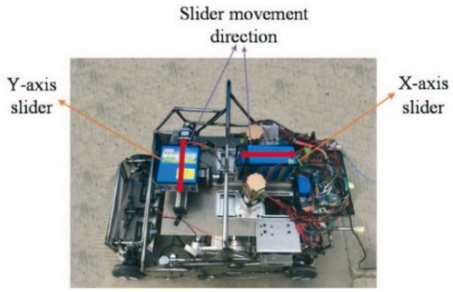

Fig. 17 Schematic diagram of the slider moving direction

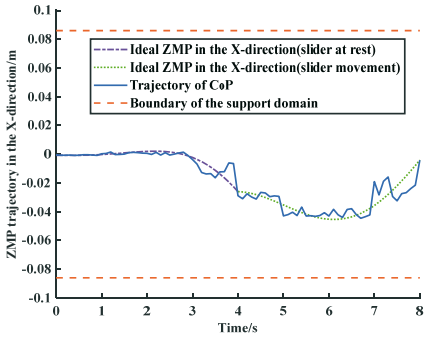

Fig. 18 CoP (centre of pressure on the sole) trajectory and ideal zero moment point (ZMP) trajectory

6. Conclusions

(1) A metamorphic mechanism for robots was studied, and a deformable robot could globally transition between vehicle and humanoid states. Compared with the traditional wheel-legged ground mobile robot, this mechanism could undergo global reconfiguration, that is, the shape, structure, centre of mass, and degrees of freedom of the system could change significantly before and after reconfiguration. Furthermore, this mechanism could achieve high speeds when in the vehicle state.

(2) The reconfiguration planning of the deformable robot was carried out, and the kinematic model of the coupled reconfiguration was established. According to the requirement that the front and rear bodies should be kept level in the reconfiguration process, a horizontal lifting motion model between the electric pusher and the lifting motor was established. The rotation law of each rotating joint was designed to satisfy the smoothness requirements. The stability criterion of the reconfiguration based on the ZMP was established.

(3) The correctness of the front body horizontal model was verified. The influence of the slider on the stability of the coupled reconfiguration was analysed. The smoothness and stability of the reconfiguration were verified again by a mechanism prototype experiment. Simulations and experiments showed that the designed deformable robot had a reasonable structure and could smoothly and stably complete the coupled reconfiguration from the vehicle state to the humanoid state.

(4) The reconfiguration motion of the deformable robot was analysed to improve the reconfiguration motion qualities outlined in the paper. The following work will be done based on the above research:

Based on the kinematic model of reconfiguration established in this paper, the mathematical models of the reconfiguration stability criteria under different conditions will be established. These conditions include reconfiguration on a horizontal road surface for different reconfiguration times, slope parking reconfiguration, and reconfiguration during driving, etc. The reconfiguration stability of the deformable robot under these conditions will be analysed.

In order to improve the stability of the reconfiguration under different conditions, and to reduce the energy consumption of the reconfiguration, high-strength and low-density carbon fiber materials can be adopted. A lightweight design will be made of the folding legs and other key components of the deformable robot based on multi-objective optimization.

The stability control algorithm applied in the metamorphic mechanism will be designed under the conditions of the driving reconfiguration or of walking. Therefore, the stability of the system under severe conditions can be improved.

DECLARATION OF CONFLICTING INTERESTS

The authors declare no potential conflicts of interest with respect to the research, authorship, and/or publication of this article.

FUNDING

The authors disclose receipt of the following financial support for the research, authorship, and/or publication of this article: This study was supported by the National Natural Science Foundation of China (Grant No. 51875148) and the Key Technologies Research and Development Program of Anhui Province (Grant No. 202104a05020040).

REFERENCES

[1] Tao Y, Wang TM; Liu H, Jiang S. Insights and suggestions on the current situation and development trend of intelligent robots, *High Technology Letters* **2019,** 29(02), 149-163.

[2] Wang SM, Xu HQ; Liu XZ, Ma HL. Research on depth recognition depth of substation intelligent patrol robot tower, *Automation and Instrumentation* **2020**, 2020(11), 73-76. 10.14016/j.cnki.1001-9227.2020.11.073

[3] Pan XX, Xu K; Wang YB, Ding XL. Design and analysis of a wheel-legged robot with a suspension system, *Robot* **2018**, 40(03), 309-320. https://dx.doi.org/10.13973/j.cnki.robot.170430

[4] Sun Y, He J; Xing Y. Multi-target coordinated control of wheel-legged Mars rover, *Acta Aeronautica et Astronautica Sinica* **2021**, 42(01), 327-339.

[5] Yue N, Li C; Han LL, Zhang YX. Scheme design of Modular Wheel-legged Lunar Robot, *Manned Spaceflight* **2020**, 25(05), 667-672. 10.16329/j.cnki.zrht.2019.05.016

[6] Qu MK, Wang HB; Rong Y. Design of Military Wheel-leg Hybrid Quadruped Robot, *Acta Armamentarii* **2018**, 39(04), 787-797.

[7] Zhao X R, Su W H; Zhang S Y. Synthesis and simulation analyses on transformable wheel-legged search and rescue robot, *Chinese Medical Equipment Journal* **2020**, 41(06), 15-20. https://dx.doi.org/10.19745/j.1003-8868.2020126

[8] Liu J, Zhang M; Chen H. Dynamic Modeling and Simulation for Obstacle-Climbing of All-Wheel-Leg-Drive Robot, *Machinery Design & Manufacture* **2015**, 2015(10), 13-17. https://dx.doi.org/10.19356/j.cnki.1001-3997.2015.10.004

[9] Zhang CY, Guo S; Zhao FQ. Motion Analysis and Gait Research of a New Wheel-legged Compound Robot, *Chinese Journal of Mechanical Engineering* **2019**, 55(15), 145-153. https://doi.org/10.3901/JME.2019.15.145

[10] Zhang N, Niu BS; Niu JY, Wu SZ; Zhang YX, Li SS; Li D. Structure modeling and error analysis of a novel wheel-legged rescue robot, *China Science Paper* **2018**, 13(16), 1871-1877.

[11] Ma ZR, Guo WZ; Gao F.: Analysis on Obstacle Negotiation of a New Wheel-legged Robot, *Machine Design & Research* **2015**, 31(04), 6-10+15. https://dx.doi.org/10.13952/j.cnki.jofmdr.2015.0129

[12] Ettore Pennestrì, Lorenzo Mariti; Pier Paolo Valentini, Mucino Victor H. Efficiency evaluation of gearboxes for parallel hybrid vehicles: Theory and applications, *Mechanism and Machine Theory* **2011**, 49: 157-176. https://doi.org/10.1016/j.mechmachtheory.2011.10.012

[13] Wettergreen D, Moreland S; Skonieczny K, et al. Design and field experimentation of a prototype Lunar prospector, *International Journal of Robotics Research* **2010**, 29(12), 1550-1564. https://doi.org/10.1177/0278364910370217

[14] Liu C, Tang XC, Yao YA, Fu ZY. Design and Analysis of a Novel Deformable Wheel-legged Robot. *Journal of Mechanical Engineering*, **2022**,58(3):65-74. https://doi.org/10.3901/JME.2022.03.065

[15] Handle. Available online: https://www.bostondynamics.com/handle (accessed on 3 Nvember **2022**).

[16] Li X , Zhou H , Feng H , et al. Design and Experiments of a Novel Hydraulic Wheel-Legged Robot (WLR) // *2018 IEEE/RSJ International Conference on Intelligent Robots and Systems (IROS)*. IEEE, **2018.** https://doi.org/10.1109/IROS.2018.8594484

[17] Oh P., Sohn K., Jang G., et al. Technical overview of team DRC-Hubo @UNLV's approach to the 2015 DARPA robotics challenge finals. *Journal of Field Robotics*, **2017**, 34(5): 874–896. https://doi.org/10.1002/rob.21686

[18] Lim J., Lee I., Shim I., et al. Robot system of DRC-HUBO+ and control strategy of team KAIST in DARPA robotics challenge finals. *Journal of Field Robotics*, **2017**, 34(4). https://doi.org/10.1002/rob.21673

[19] Jin GG, Gao F, Ding X L. On classification and configuration analysis for metamorphic mechanisms. *Mechanical Science and Technology for Aerospace Engineering*, **2005**(07):764-767.

[20] He X T, Cheng Y, Huang Z, et al. Transformation of homogeneous coordinates and its application in the analysis of spatial mechanism. *Journal of Beijing University of Chemical Technology (Natural Science)*, **1999**(01):43-46.

[21] Li X et al. Stable jump control for the wheel-legged robot based on TMS-DIP model. *Industrial Robot: the international journal of robotics research and application*, **2021**, 49(2): 212-225. https://doi.org/10.1108/IR-04-2021-0083

[22] Chen ZH et al. Towards Hybrid Gait Obstacle Avoidance for a Six Wheel-Legged Robot with Payload Transportation. *Journal of Intelligent &Robotic System*, **2021**,102(3). https://doi.org/10.1007/s10846-021-01417-y

[23] V. Klemm et al., "Ascento: A Two-Wheeled Jumping Robot," *2019 International Conference on Robotics and Automation (ICRA)*, **2019**:7515-7521. https://doi.org/10.1109/ICRA.2019.8793792

[24] Zhao L., Yu Z., Chen X., Huang G., Wang W., Han L., Qiu X., Zhang X., Huang Q. System design and balance control of a novel electrically-driven wheel-legged humanoid robot. *In Proceedings of the 2021 IEEE International Conference on Unmanned Systems (ICUS)*, Beijing, China, 1–5 October **2021**: 742–747. https://doi.org/10.1109/ICUS52573.2021.9641385

[25] He XT, Cheng Y, Huang Z, et al. Transformation of homogeneous coordinates and its application in the analysis of spatial mechanism[J]. *Journal of Beijing University of Chemical Technology (Natural Science)*,**1999**(01):43-46.

[26] Liao B, Shang J Z, ERNEST Appleton, et al. Kinematics Analysis of a 5-DOF Anthropopathic Arm Based on Sarrus Linkage[J]. *Chinese Journal of Mechanical Engineering*, **2013**,49(03):18-23. https://doi.org/10.3901/JME.2013.03.018

[27] Ma D, Liu Y, Ye Z, Wei Y, Liu J. Analysis of the tooth surface contact area of a circular-arc-tooth-trace cylindrical gear under load [J]. *Transactions of FAMENA*, **2021**, 45(1):79-94. https://doi.org/10.21278/TOF.451018220

[28] Xiang T, Yi J, Li W. Five-axis numerical control machining of the tooth flank of a logarithmic spiral bevel gear pinion [J]. *Transactions of FAMENA*, **2018**, 42(1):73-84. https://doi.org/10.21278/TOF.42107

[29] Dimitar D, Iliya Z, Nikolay M. Dynamic error and methods for its elimination in systems for measuring parameters of moving objects [J]. *Transactions of FAMENA*, **2021**, 45(4):55-70. https://doi.org/10.21278/TOF.454029721

[30] Zhang X, Liang Z. Comparison of conventional double-helical and curvilinear cylindrical gear drives in terms of transmission errors and stress [J]. *Transactions of FAMENA*, **2021**, 45(3):1-18. https://doi.org/10.21278/TOF.453016020

[31] Hu WZ. Research on motion planning method of humanoid walking Robot, *National University of Defense Technology*, **2002**.

[32] Yu ZW, Wang LQ; Han JH. Walking stability in bipedal robots, *Journal of Harbin Engineering University* **2009**, 30(11), 1285-1290.

[33] Mahmood I, Martinez-Hernandez U. A model identification approach to quantify whole-body vertical vibrations impact on limb compliant dynamics and walking stability, *Medical Engineering & Physics (prepublish)* **2020**,80. https://doi.org/10.1016/j.medengphy.2020.04.005

[34] Lin DD, Liu L, Zhao JD. Measurement and study on ZMP-CoP of the biped walking robot, *Rob*ot, **2004**(04):368-372+379.

Submitted: 21.5.2022

Accepted: 24.4.2023

Jun Liu*
Jiandang Xing
Xiaodong Ruan
Jian Song
Di Wu
School of Automotive and Traffic Engineering
Hefei University of Technology, Hefei, China
*Corresponding author:
ljun@hfut.edu.cn